3D intrusions transport active surface microbial assemblages to the dark ocean

Mara A. Freilich[a,b,c,d,1] (ID), Camille Poirier[e], Mathieu Dever[f], Eva Alou-Font[g] (ID), John Allen[g], Andrea Cabornero[g], Lisa Sudek[h], Chang Jae Choi[e], Simón Ruiz[i] (ID), Ananda Pascual[i], J. Thomas Farrar[f], T. M. Shaun Johnston[b] (ID), Eric A. D'Asaro[j], Alexandra Z. Worden[e,h,k,1] (ID), and Amala Mahadevan[f,1] (ID)

Subtropical oceans contribute significantly to global primary production, but the fate of the picophytoplankton that dominate in these low-nutrient regions is poorly understood. Working in the subtropical Mediterranean, we demonstrate that subduction of water at ocean fronts generates 3D intrusions with uncharacteristically high carbon, chlorophyll, and oxygen that extend below the sunlit photic zone into the dark ocean. These contain fresh picophytoplankton assemblages that resemble the photic-zone regions where the water originated. Intrusions propagate depth-dependent seasonal variations in microbial assemblages into the ocean interior. Strikingly, the intrusions included dominant biomass contributions from nonphotosynthetic bacteria and enrichment of enigmatic heterotrophic bacterial lineages. Thus, the intrusions not only deliver material that differs in composition and nutritional character from sinking detrital particles, but also drive shifts in bacterial community composition, organic matter processing, and interactions between surface and deep communities. Modeling efforts paired with global observations demonstrate that subduction can flux similar magnitudes of particulate organic carbon as sinking export, but is not accounted for in current export estimates and carbon cycle models. Intrusions formed by subduction are a particularly important mechanism for enhancing connectivity between surface and upper mesopelagic ecosystems in stratified subtropical ocean environments that are expanding due to the warming climate.

oceanography | microbial ecology | carbon export | mesopelagic | mesoscale

Surface ocean carbon fixation by photosynthetic planktonic microbes generates particulate organic carbon (POC) that fuels marine ecosystems (1). A portion of this POC is exported to the underlying dark ocean where it is a critical energy source for heterotrophic organisms. However, particularly in the subtropics, the mechanisms for export of POC are unclear (2, 3) despite the fact that a major fraction of global primary production occurs in these regions (1). In subtropical regions, the sunlit photic zone is dominated by picophytoplankton (diameters < 3 μm) that are nonsinking due to their small sizes. These unicellular microbes include the picocyanobacteria, *Prochlorococcus* and *Synechococcus*, as well as picoeukaryotes, and succeed in oligotrophic subtropical gyres because their small size is advantageous for nutrient acquisition under limiting conditions (4, 5). Importantly, picophytoplankton-dominated environments are expanding due to surface ocean warming, which strengthens vertical stratification and induces nutrient-limiting conditions (6, 7).

Contrary to the expectation that picophytoplankton cells would not arrive intact in the dark mesopelagic (depths ≥ 200 m) due to the hundreds of days it would take for them to sink, DNA, photosynthetic pigments (e.g., chlorophyll *a*), or cells of cyanobacteria have occasionally been found in subtropical mesopelagic sediment traps and samples (8–10). Various mechanisms for picophytoplankton packaging, including proposed aggregation of dead cells during viral lysis or in zooplankton fecal matter are among explanations for enhanced export efficiency. These mechanisms may explain some of the observed picophytoplanktonic material at dark depths, depending on degradation rates and other factors. Additionally, physical processes involving vertical movement of water masses, such as polar thermohaline-driven sinking (11) and advection by oceanic surface mixed layer eddies (12), result in export of picophytoplankton and oxygen from the surface. The surface-enhanced submesoscale (1 to 10 km scale) dynamics that generate mixed layer eddies and filaments are found in regions with deep surface mixed layers and strong surface forcing, such as the subpolar North Atlantic, coastal upwelling fronts, and the Southern Ocean (12, 13). However, the shallowness of the mixed layer in the subtropics results in weaker submesoscale dynamics (14). Further, since subtropical surface waters are nutrient-depleted, phytoplankton biomass is often concentrated below the mixed layer, particularly in the summertime, making it less prone to export by mixed layer processes.

Significance

Particulate organic carbon (POC) formed by photosynthesis in the sunlit surface ocean fuels the ecosystems in the dark ocean below. We show that mesoscale fronts and eddies, which are ubiquitous physical features in subtropical oceans, generate three-dimensional intrusions connecting the surface to deep ocean. Intrusions are enriched in total POC due to enhancement of small, nonsinking photosynthetic plankton and free-living bacteria that resemble surface microbial communities. Flow-driven export of POC, estimated using an approximation of eddy physics, is the same order of magnitude as export by sinking POC, which was previously thought to dominate export. These observations reveal coupling of surface and deep ocean productivity and biodiversity and give insight into mechanisms by which the ocean transports carbon to depth.

By contrast, mesoscale (10 to 100 km scale) processes that generate sloping density surfaces (fronts) are ubiquitous in the subtropics. Mesoscale features can also facilitate relatively rapid submesoscale vertical motion (order 100 m d^{-1}) but their contributions to POC export from the photic zone are generally not considered. Building on prior understanding of the impact of frontal dynamics on primary production, mesoscale vertical motion, and vertical transport of chlorophyll in the subtropical Mediterranean Sea (15–18) and other mid-latitude regions (19–22), we undertook biophysical observations to identify signatures of active submesoscale vertical exchanges that lead to export and analyze resident microbial communities using flow cytometry and molecular analyses. Together, these measurements enabled us to trace three-dimensional chlorophyll-containing intrusions to the upper mesopelagic and determine their environmental origins in the photic zone (upper 70 m). We observed intact picophytoplankton cells in the aphotic zone at mesoscale fronts in this region. We then probed differentiated microbial assemblages and quantified their contributions to carbon export in the upper mesopelagic. The results demonstrate that alongside carbon export from picophytoplankton cells, there is a significant, but previously unrecognized, export of heterotrophic bacteria, and their carbon, in a nondecayed state via the 3D intrusions. Moreover, two enigmatic, broadly distributed marine bacterial groups, Marinimicrobia (SAR406) and Parvibaculales (OCS116) (23–25), appear to be stimulated in the intrusions.

Drawing together these lines of evidence, we demonstrate that intrusions enhance picoplankton carbon export and alter microbial diversity and composition through surface-to-mesopelagic pathways. The varied outcomes of microbial interactions in the upper mesopelagic may allow for enriched genetic and metabolite exchanges between microbial taxa from different habitats, alongside delivering POC that differs in nutritional composition and lability from background mesopelagic waters. Upon establishing the importance of this mechanism for picoplankton export and community structure, we explored its potential significance at a global level, finding that intrusion dynamics contribute as much carbon to the upper mesopelagic as estimated sinking in subtropical regions.

Results and Discussion

Chlorophyll-Containing Intrusions in the Dark Ocean Are Formed by Frontal Subduction. While intrusion features that subduct chlorophyll to the upper mesopelagic have been documented in the Western Mediterranean Sea (15, 16, 18), the biophysical dynamics and ecological significance of these chlorophyll features are not understood. Therefore, we conducted ship-based expeditions in July 2017, May to June 2018, and March to April 2019 wherein oceanic density fronts in the Western Mediterranean Sea were repeatedly transected (Fig. 1A). Fronts in this region partition relatively fresh, cool, and buoyant Atlantic waters that enter the Alborán Sea, from saltier, warmer, and denser Mediterranean waters (*SI Appendix*, Fig. S1). We measured salinity, temperature, and bio-optical properties at approximately every meter from the surface to 200 m depth, using towed profilers. This was performed as the ship transited orthogonal to strong frontal flows that separate the Western and Eastern Alborán gyres and are known to evolve on timescales of weeks to months (26).

The chlorophyll and biomass maxima coincide within the photic zone (Fig. 1 B and C and *SI Appendix*, Figs. S2 and S3), (based on in vivo chlorophyll *a* fluorescence and optical backscatter at 700 nm), both in our observations and in previous
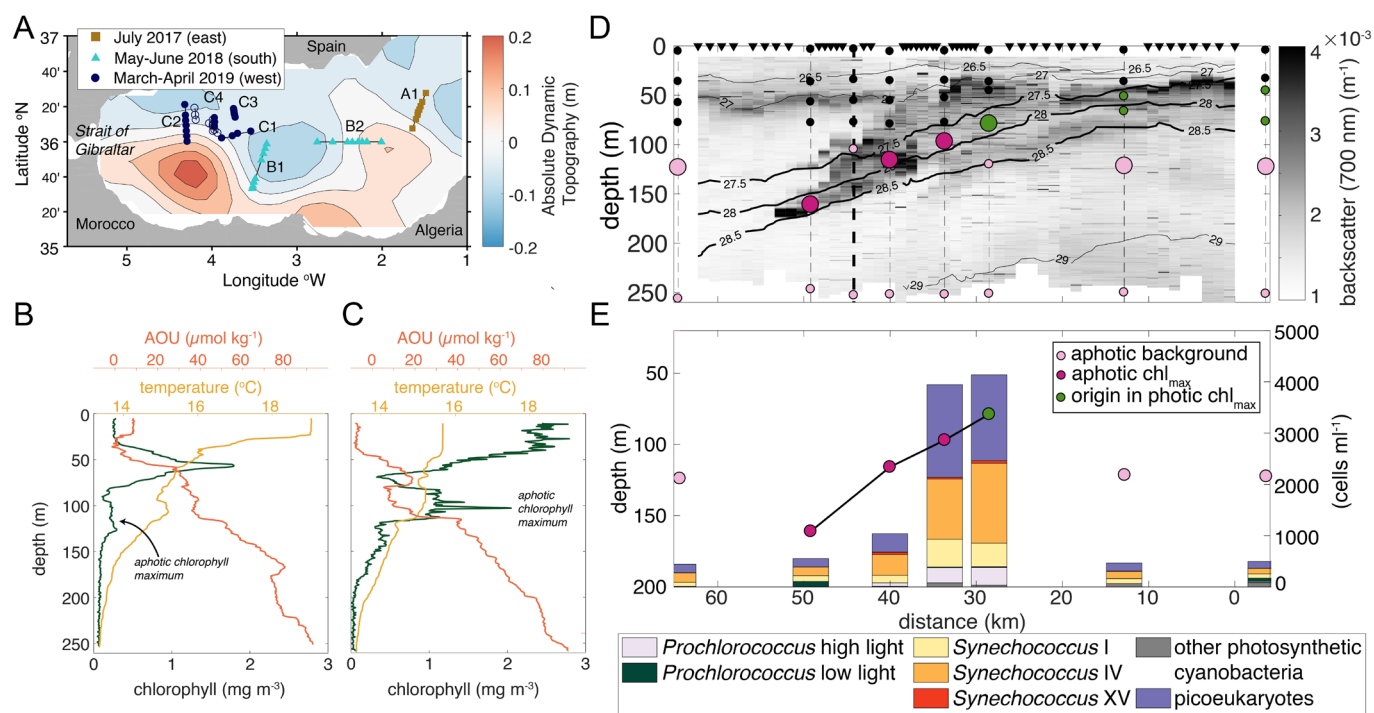

Fig. 1. Chlorophyll maxima below the Mediterranean Sea photic zone are formed by surface-derived intrusions. (A) Eastern and Western Alborán gyres showing ship transects (lines) with measurements and locations of water sampling (symbols) and where molecular analyses and flow cytometry were performed (filled symbols); the background shows absolute dynamic topography (ADT) on May 25, 2018, illustrating general gyre positioning. (B and C) Chlorophyll fluorescence, apparent oxygen utilization (AOU), and temperature from two representative profile types in summer (May 2018) (B) and winter/spring (March 2019) (C), with the aphotic chlorophyll maxima (indicated between 100 and 150 m) where co-occurring inversions are observed relative to background trends in temperature and AOU. (D) Example two-dimensional section across transect B2 (panel A), with 0 km being at the western edge. Locations of EcoCTD casts (triangles), standard CTD casts (dashed lines), and backscatter (grayscale) indicated. The panel B cast is highlighted for reference (bold dashed line). Molecular samples (dots) are taken from the photic zone (black dots), ACM (dark pink), origin waters of the ACM, namely the chlorophyll maximum on the dense side of the front (green), and the aphotic background (light pink); larger dots represent those displayed in panel E. (E) Phytoplankton abundances and community composition by V1–V2 16S rRNA gene ASV analyses along transect B2 at depths representing the intrusion (green and dark pink connected by a line) and in background samples (light pink; i.e., same depth as intrusions but outside).

observations of this region (27). This established that peaks in chlorophyll fluorescence in the photic zone were associated with increased biomass, and were not solely the result of phytoplankton photoacclimation. More generally, two types of "classical" water column structures were observed within the photic zone: i) a deep chlorophyll maximum (DCM) at the top of the nutricline and beneath the mixed layer (Fig. 1*B*; mixed layer depth was 5 to 20 m and 1% light level was at 50 to 60 m depth) during warmer periods when the photic zone exhibits thermal stratification, as observed in May to June 2017 and July 2018; and ii) a well-mixed surface layer with relatively even chlorophyll distributions between 0 and 70 m during the March to April 2019 expedition (Fig. 1*C*; 1% light level was at 60 to 70 m). Such seasonal patterns in the vertical structure are similar to those of the Atlantic and Pacific subtropical gyres (28). In some subtropical regions, DCMs can arise from photoacclimation and care should be taken in interpreting biomass gradients relative to chlorophyll gradients.

Strikingly, on multiple transects, we also observed secondary maxima in chlorophyll within the aphotic zone (deeper than 90 m), beneath the seasonally varying surface mixed layer as identified by uniform density (e.g., Fig. 1 *B* and *C*). The secondary, aphotic chlorophyll maxima (ACM) co-occurred with secondary maxima in optical backscatter at 700 nm and beam transmission (another proxy for POC), alongside secondary minima in AOU or, equivalently, maxima in oxygen saturation, and warm temperature anomalies on isopycnals (spice anomalies) (Fig. 1 *B–D*). The concurrent ACM and minima in AOU were indicative of water being subducted from the photic zone on time scales short enough that oxygen levels remained high and fluorescing chlorophyll was present in the dark.

The anomalous chlorophyll features and associated water mass characteristics were inconsistent with mechanisms that have been previously suggested for ACM formation in other subtropical regions. Photoautotrophic growth is not sufficient to drive the observations, given the lack of sunlight and because the co-occurring peaks in chlorophyll and beam attenuation or backscatter indicate that phytoplankton photoacclimation alone did not generate the maxima (*SI Appendix*, Fig. S4). Likewise, vertical mixing does not generate secondary maxima or minima, or the observed spice anomalies. Moreover, sinking POC would not generate the anomalously high oxygen concentrations observed below the photic zone. Thus, the ACMs, which are seen in contiguous profiles at the same (or similar) density are identified to be along-isopycnal intrusions.

To pursue the biological dynamics and origins of the observed ACMs, we examined the nature of the material contributing to ACM signatures in a biological and ecological framework. To this end, we turned to the full complement of biological, physical, and bio-optical measurements recovered at a horizontal spacing of 1 to 10 km on 10 frontal crossings (Fig. 1*A*), which offers a highly resolved picture of microbial community variability. By observing downward CTD cast data in real-time, we adaptively sampled 6 depths during the upcast, which included a) the ACM, when present, b) regions of high chlorophyll *a* and biomass in the photic zone; either the well-mixed high chlorophyll layer within the surface mixed layer or DCM in the stratified region below the surface mixed layer, c) photic zone depths not within a chlorophyll maximum, and d) aphotic, upper mesopelagic background samples from below the photic zone (but not within an ACM). Our sampling also targeted consistent density surfaces on a given cross-frontal transect when possible, as advective transport occurs along isopycnals, or surfaces of constant density. While we first identify ACMs based on a chlorophyll fluorescence signal, we only classify features as ACMs if they have inversions in the vertical in at least one other

biogeochemical property as well (*Materials and Methods*). Cell enumeration by flow cytometry in these features consistently demonstrated that both photosynthetic eukaryotes and cyanobacteria had higher abundances in the ACM compared to the background upper mesopelagic water, as exemplified in Transect B2 (Fig. 1 *D* and *E* and SI *Appendix*, Fig. S5). The combined biological and biophysical analyses of cross-frontal transects, showing co-occurrence of ACMs and AOU minima in contiguous vertical profiles alongside corresponding changes in phytoplankton abundances, suggest they are part of coherent intrusions that provide a 3D pathway for transport from the photic zone to the dark ocean.

The anomalies that characterized intrusions, specifically of chlorophyll and AOU, became weaker with increasing depth, as did the spice anomalies, although to a lesser degree (e.g., Fig. 1 *D* and *E* and *SI Appendix*, Fig. S5). Notably, the proportion of cyanobacteria among the picophytoplankton increased with depth relative to picoeukaryotes (*t* test *P* = 0.0023, CI = [1.0623, 1.2598] where 1 is no change). This may be attributable to a differential loss of picoeukaryotes due to higher mortality rates (5), or possibly greater persistence of picocyanobacteria in dark conditions (29). Changes in biological properties with depth within intrusions relate to the decay of chlorophyll and respiration of organic matter, as well as mixing with surrounding waters. In contrast, spice is unaffected by bio-chemical processes and traces water masses as they are stirred by the flow; its anomalies are attenuated only by mixing. Despite weakening signatures, we found that phytoplankton within the intrusions comprise intact cells with classical fluorescence and light scattering properties that differ from dead picophytoplankton cells and aphotic communities outside intrusions. Thus, while modifications in intrusion signatures indicate that deeper parts of intrusions are older, having left the photic zone prior to shallower parts, we also infer from the intact cells that there is transport in the intrusions on timescales of days. This transport connects photic zone communities to the mesopelagic and is likely achieved through submesoscale dynamics.

Our findings point to export of phytoplankton on spatial and temporal scales that are unlikely to be achieved through mesoscale-driven vertical transport alone, which was previously used to explain chlorophyll intrusions in the Mediterranean Sea. Intrusions are 3D features that appeared to originate in 1 to 10 km patches along the fronts and extend downward at least 200 m in the vertical and 10 s of kilometers transversely, along the sloping density surfaces that constitute the front. The features can extend approximately 100 km in the direction of the front because the along-front velocity is about 1,000 times larger than the vertical velocity. This spatial structure is emblematic of the coupling between surface-enhanced submesoscale processes and deeper mesoscale dynamics, which can locally intensify fronts and generate more rapid subduction, as established by our modeling efforts herein (*SI Appendix*, SI Text) and previously (16, 19, 30). Together, the modeling studies demonstrate downward instantaneous vertical velocities of up to 100 m d^{-1}, even below the surface, generating sustained time-integrated vertical transport (subduction) in intrusions in excess of ~10 m d^{-1} (16, 30, 31). The mechanism identified in our subtropical study region therefore results in transport to greater depths than the wintertime mixed layer in both winter and summer. This prevents remixing to the surface at the annual onset of deep mixing, leading to year-round episodic export of picophytoplankton to the upper mesopelagic. Collectively, the intrusions characterized herein are generated by different physical processes than those previously invoked for small phytoplankton export, which rely on mixed layer processes and transport POC only as deep as the wintertime mixed layer depth (12).

Intrusions Transport Picophytoplankton Communities from Surface or DCM Waters to the Upper Mesopelagic. We next aimed to more precisely identify the origins of the picophytoplankton communities that reached aphotic depths within the intrusions. To this end, we examined phytoplankton community composition in 221 transect samples using phylogenetic analysis of V1-V2 16S rRNA gene amplicon sequence variants (ASVs), which capture cyanobacteria and plastids from eukaryotic phytoplankton (28, 32). In addition, flow cytometry (FCM) was used to determine phytoplankton cell abundances. As expected, picophytoplankton groups in the photic zone exhibited both depth-related patterns and seasonality in cellular abundances and community composition related to the seasonal changes in water column structure on our transects and consistent with patterns reported in the Western Mediterranean Sea and other subtropical locations (28, 32–34). With respect to intrusions, water column structure appeared to influence the depth of origin. For example, in Transect B2, which came from a stratified period (May to June, Fig. 1*D*), communities from the DCM, rather than the surface, appeared to be the origins of the ACM picophytoplankton cells and POC. Specifically, *Synechococcus* clades I and IV and eukaryotic cells were the dominant picophytoplankton in the ACM and their relative abundances were similar in the DCM and ACM (Fig. 1*E*), while the surface community was dominated by *Synechococcus* clade IV. In contrast, in March to April 2019, when the mixed layer was near its annual maximum depth, the intrusion that generated the ACM appeared to be sourced from the surface mixed layer, with the ACM and surface communities being similar (*SI Appendix*, Fig. S5).

Across all sampled transects, communities within an intrusion were more similar to communities in the photic chlorophyll maximum than background waters, despite the decay in the "strength" of intrusion signals during descent (Fig. 1*E* and *SI Appendix*, Fig. S5), which potentially complicates identification of source waters. Hierarchical clustering based on community composition grouped communities sampled from the ACM primarily with microbial communities from the well-mixed surface layer or DCM (when present) on the dense side of fronts (Fig. 2*A*). This suggests that intrusions connect chlorophyll maxima in the photic zone to the dark ocean, regardless of the particular depth of that chlorophyll maximum. Due to differences in origin communities from transect to transect, the totality of intrusion communities does not collectively converge to a single unique community composition. The depth distributions of samples in each cluster demonstrate that ACM communities are significantly deeper in the water column than communities within the same cluster (30 to 50 m deeper than the depth of origin, $P < 10^{-5}$, Fig. 2*B*). The limited change in community composition, as well as physical parameters, between photic zone and intrusion samples suggests that advective transport to 100 to 200 m occurs over a few days (< 10 d). Our high-resolution comparative analyses of picophytoplankton community composition served as a sensitive tracer of along-isopycnal vertical transport and connectivity between the ACM and source water communities. The results further establish that intrusions drive export of picophytoplankton from photic zone chlorophyll maxima operating on a year-round basis, rather than just during physically energetic periods of the year, like winter.

POC Transported by Intrusions into the Upper Mesopelagic Includes a Dominant Signal from Nonphotosynthetic Bacteria. The intrusions transported picophytoplankton to the dark ocean, raising questions regarding the total flux of carbon to the upper mesopelagic from intrusions. Using beam transmission data as a proxy for POC, we found that nearly all instances of high POC in the aphotic zone at the observed fronts were associated with

ACMs that result from intrusions, rather than sinking (Fig. 3 *A* and *B*). The intrusions generated substantial patchiness in POC in the upper mesopelagic. This was most evident in the probability density distribution of beam transmission-derived POC differentiated into "intrusion" and "background" mesopelagic samples with the same depth distribution. The total POC within intrusions averages twice that of background mesopelagic waters (Fig. 3 *A* and *B*).

The adaptive sampling of intrusions enabled us to quantify contributions of picophytoplankton groups to physically driven export. The contribution of *Prochlorococcus*, *Synechococcus*, and picoeukaryotic phytoplankton to carbon export is assessed using cell abundances and established carbon conversion factors. This reveals that across all seasons studied, there is a significant enhancement of carbon from picophytoplanktonic cells in aphotic regions of the intrusions compared with background mesopelagic waters at the same depth, where very few picophytoplankton are observed (Fig. 3*C*). Picophytoplankton biomass in the aphotic intrusions is of comparable magnitude and composition to the photic zone communities.

Because the intrusion export mechanism also carries heterotrophic microbes that co-occur with the picophytoplankton from the photic zone, we enumerated them by flow cytometry. The process of subduction has important consequences for heterotrophic bacteria, since they are even smaller than picophytoplankton and sink more slowly. Nonphotosynthetic microbes averaged $8.7 \times 10^5 \pm 3.2 \times 10^5$ cells mL^{-1} in the photic zone and, due to their high abundance, comprised about half of the total microbial POC in sunlit waters (when using established cellular carbon content conversions) (Fig. 3 *C* and *D*), akin to data from prior subtropical studies (35). Subduction of these abundant bacteria resulted in abundance peaks in intrusions ($5.6 \times 10^5 \pm 1.5 \times 10^5$ cells mL^{-1}) that were nearly twice the number seen in background upper mesopelagic samples ($3.1 \times 10^5 \pm 7.8 \times 10^4$ cells mL^{-1}) at the same depth in the aphotic zone (Fig. 3*D*). Moreover, their biomass contributed as much, or more, POC to advective export as all the picophytoplankton groups combined (Fig. 3 *C* and *D*).

The substantial POC contribution by heterotrophic bacteria was initially surprising to us, since the intrusions herein were identified via their elevated chlorophyll. Indeed, the presence of anomalously high chlorophyll and backscattering below the photic zone (12, 13) has been considered almost exclusively through the lens of phytoplankton and the importance of phytoplanktonic advective export in the biological pump. However, our findings are consistent with the fact that in the nutrient-limited subtropics, nonphotosynthetic bacteria have much higher abundances in the photic zone—where intrusions originate—than at depth (36). Thus, the intrusion export mechanism represents an "optimal" export for heterotrophic bacteria, matching their peak biomass. Moreover, reevaluation of the relationship between total POC (beam transmissometer-derived) and microbial POC (cell counts-derived) showed that when biomass of picophytoplankton is summed with that of heterotrophic bacteria, there is a significant correlation with total POC ($R^2 = 0.42$ (spring), 0.46 (summer), $P < 10^{-14}$), stronger than with just phytoplankton ($R^2 = 0.39$ (spring), 0.42 (summer), $P < 10^{-11}$), with seasonally dependent offsets that are likely connected to amounts of POC from intact cells versus detrital particles (*SI Appendix*, Fig. S7). Even considering the substantial uncertainty in the carbon content per cell, which is particularly large [up to ±50%; (37–39)] for the diverse eukaryotic and heterotrophic bacteria classes (*SI Appendix*, Fig. S7), the heterotrophic bacteria make a substantial contribution relative to phytoplankton. The identification of a marked enrichment of carbon in the upper mesopelagic due to heterotrophic bacterial communities that are transported within
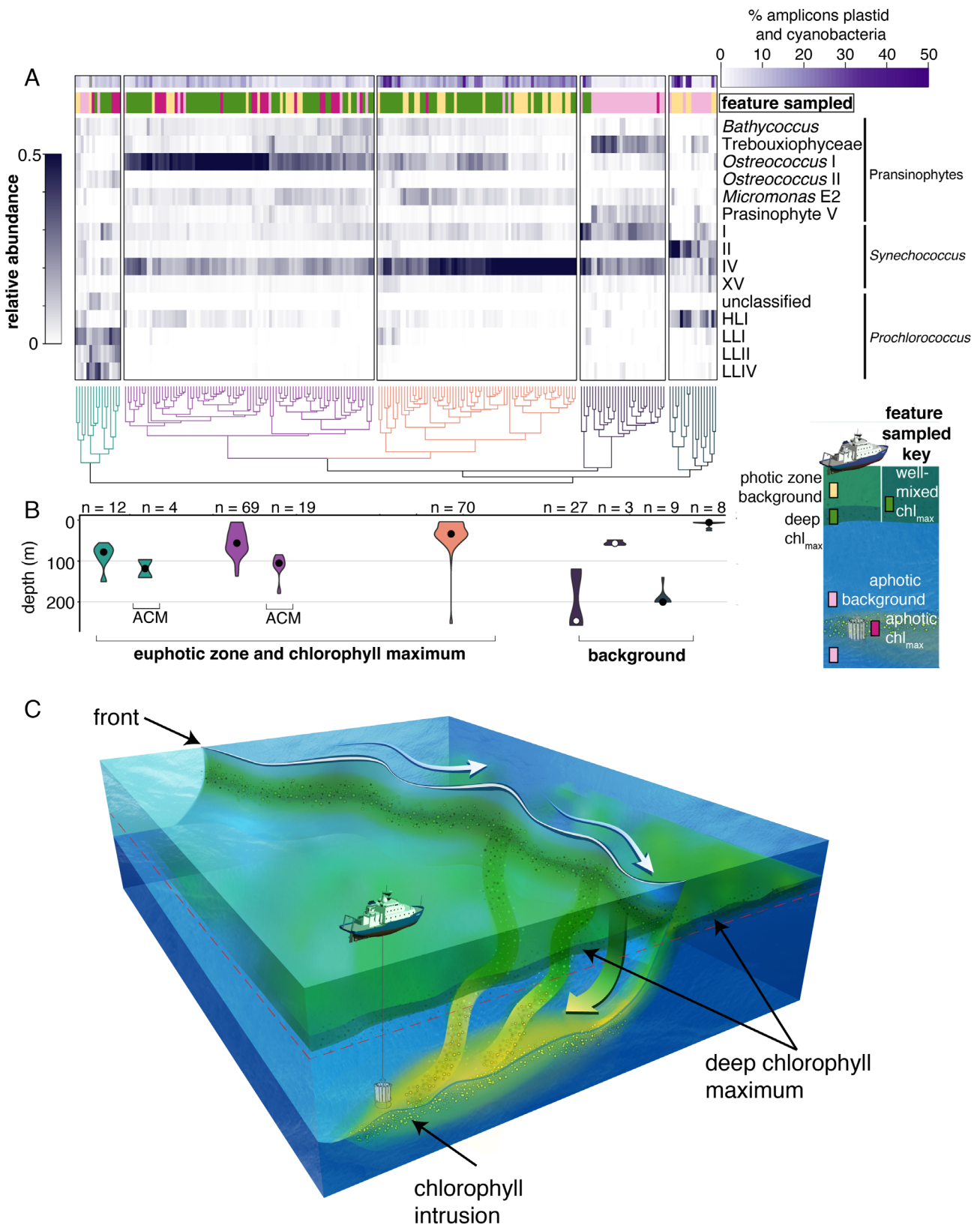
Fig. 2. Surface ocean picophytoplankton communities are exported to the aphotic zone via intrusions. (*A*) Hierarchical clustering of picophytoplankton taxa identified using phylogenetic placement of V1–V2 16S rRNA gene ASVs (see *SI Appendix*, Fig. S8 for phytoplankton taxa of lesser relative abundance). Each colored cluster in the dendrogram is significant (*P* < 0.05). First, we tested the extent to which diversity had been saturated in our deep sequencing efforts; analysis of rare taxa was not undertaken due to lack of saturation in some samples (*SI Appendix*, Fig. S9). The top horizontal bar (purple) indicates the percentage of ASVs from cyanobacteria and photosynthetic eukaryotes out of the total number of amplicons, which includes sequences from heterotrophic bacteria; the two left-most clusters show extremely low percentages of sequences from phytoplankton, as expected of classical dark ocean samples. The second horizontal bar indicates the sampled feature type. The heat maps shows the relative abundance of each taxa. (*B*) Respective depth distribution of samples in selected clusters (shown by violin plots corresponding in color to clusters above) represented as the mean and distribution of samples (n indicates the number of samples). (*C*) Schematic of a frontal system with a deep chlorophyll maximum and an aphotic chlorophyll-containing intrusion. Intrusions are coherent, three-dimensional features with multiple origin locations along the front. Sampling occurred in transects capturing a cross-section of a three-dimensional system.
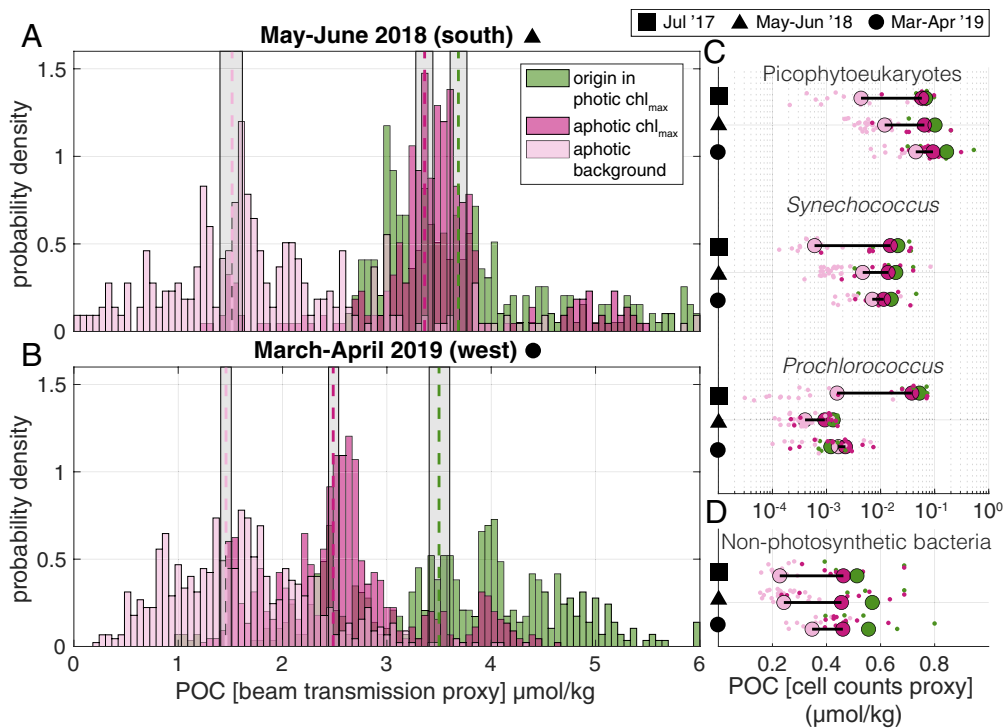
Fig. 3. Intrusions are enhanced in POC at depth with unexpectedly large contributions from nonphotosynthetic bacteria. (*A* and *B*) Probability density functions of POC concentration estimated for summer 2018 and spring 2019, respectively, from transmissometer profiles within the ACM (dark pink), background (light pink, randomly sampled from outside the ACM to have the same depth distribution), and origin waters (green, high chlorophyll regions in the photic zone with density ranges of ACM). The geometric mean of POC distributions in the ACM, origin, and background are indicated (dashed lines, color coding on panel) with gray shading for the 95% CI (note, beam transmission and optical backscatter were not available for 2017). (*C*) POC amount contributed by each major phytoplankton group within ACMs, photic chl max, and aphotic background over the three expeditions (indicated by black symbols on the *y*-axis). Note log scale (*x*-axis). (*D*) POC contributed by nonphotosynthetic bacteria is greater than phytoplankton. For *C* and *D,* POC estimates are based on flow cytometry analysis of intact cells and established conversion factors; colors are as in panel *A*. Note that improved data on taxon-specific cellular carbon content will be an important future step for improving quantitative estimates of taxon-specific carbon export.

3D intrusions modifies the current paradigm of microbial carbon export.

Enigmatic Nonphotosynthetic Bacterial Groups Are Stimulated in Intrusions. Differences in the physiological and biogeochemical impact of transport into the dark ocean along intrusions are notable for heterotrophic bacteria in comparison with picophytoplankton. The latter are at life's end, providing important labile food resources for predators and bacteria, and potentially for export to greater depths. In contrast, some nonphotosynthetic bacteria have the possibility to continue growing at depth, in addition to having differentiated roles in remineralization of POC and attenuation of organic matter (28, 36). Thus, along with their large export contribution in terms of carbon, heterotrophic microbes perhaps have the greatest impacts on biogeochemical and ecological transformations along intrusions.

Subtropical nonphotosynthetic bacterial communities are dominated by SAR11 in the photic zone (28). Here, we observed dominance by SAR11 clade Ia in the photic zone, while SAR11 clades Ib and II and SAR324 had the highest relative abundances in aphotic communities (Fig. 4*A*). Heterotrophic microbial communities reflected the surface origin communities in a manner that differed from the phytoplankton communities. Specifically, the intrusions increased the aphotic zone heterotrophic community complexity and multiple nonphotosynthetic bacterial taxa appeared to systematically respond to subduction in differing ways (Fig. 4*A*). Differential relative abundance analysis on the ASV data revealed 16 nonphotosynthetic bacterioplankton ASVs with significant increases in the ACMs over both aphotic background waters and

intrusion origin waters. Among these were SAR406 (8 ASVs), the *Verrucomicrobia* lineages Arctic 97B-4 (4 ASVs) and MB11C04 (marine groups) (1 ASV), and OCS116 clade members (3 ASVs). The response of *Verrucomicrobia* and OCS116 to labile material from phytoplankton blooms has been noted previously (23, 40, 41), supporting the idea that they preferentially respond to the decay of the relatively high phytoplankton biomass in intrusions. SAR406 have also been observed to respond to environmental variability at mid-depth in other regions, but with less clear triggers (25). This broad uncultivated alphaproteobacterial lineage exhibits diverse roles in sulfur and nitrogen metabolism, based on metagenomic analyses, with some clades even encoding nitrous oxide reductase. Thus, the biogeochemical transformations they perform within the intrusions appear complex and likely shift the repertoire of the collective metabolisms present in the aphotic zone.

Subduction through intrusions, as described herein, impacts the functional and metabolic diversity of the aphotic zone differently than processes that are conventionally invoked for explaining vertical connectivity [e.g., convection, active transport by zooplankton, and sinking detrital particles (42–44)]. The more rapid timescales of intrusions, and coherence of the water mass and environmental conditions, contribute to the living nature of exported cells and growth of activated community members as they experience transitions in light and organic matter lability during transport.

Vertical Flux of POC Due to Intrusions Can Rival Sinking Flux. We next aimed to estimate POC contributions to the dark ocean via intrusions by combining multiple datasets and process study modeling for the frontal setting in a global context. Using
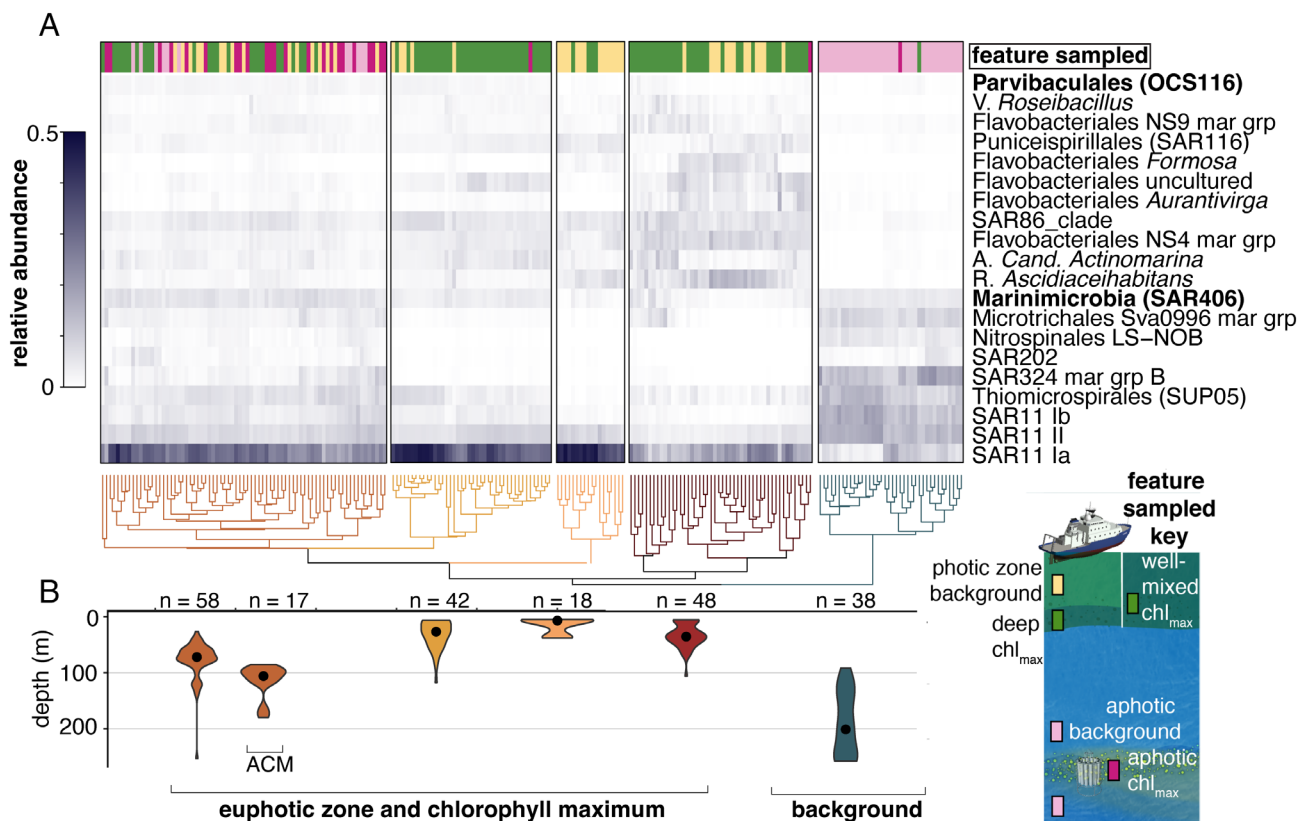
Fig. 4. Specific nonphotosynthetic bacterial lineages appear to respond to intrusion conditions, reshaping community structure. (*A*) Hierarchical clustering of nonphotosynthetic bacterioplankton distributions with taxonomy determined using V1-V2 16S rRNA gene ASVs and established databases. The percentage contribution to total amplicons of the most relatively abundant taxa across all samples is shown in the heat map (grayscale). Bacterial taxa that were differentially more abundant in intrusions based on statistical analysis are denoted (bold lettering) and indicate enrichment in the ACM relative to the upper mesopelagic background and source photic-zone waters. The sampled feature is shown in the bar above the heatmap and is subtly different than that of picophytoplankton due to differences in hierarchical clusters influenced by enrichment of heterotrophs that appear to respond to the intrusion conditions. Each colored cluster is significant (*P* < 0.05). (*B*) Respective depth distribution of samples in selected clusters (shown by violin plots corresponding in color to clusters above) represented as the mean and distribution of samples (n indicates the number of samples). Nearly all ACM samples are in the same cluster and ACM samples are found deeper than other communities in this cluster.

the observed POC anomalies in intrusions and a conservative estimate of the vertical velocity as 10 m d^{-1}, we estimate the local flux in Western Mediterranean Sea intrusions is on the order of 100 mg C m^{-2} d^{-1}.

Subduction promotes two-way connectivity between photic and aphotic communities. Therefore, to obtain the net carbon flux, it is necessary to integrate in space and time over regions and episodes of positive and negative flux (i.e. upwelling and downwelling). We used a submesoscale resolving process study ocean model (PSOM) initialized with the observed hydrographic conditions and POC distribution (*SI Appendix*, SI Text 9). Certain aspects of the large-scale Mediterranean circulation are particular, resulting in quasi-stationary fronts that have previously been thought to be critical for generating intrusions (15, 16, 26). The process study model we use here generalizes the frontal export process beyond the quasi-steady topographically influenced conditions in the Alborán Sea and instead quantifies the influence of globally relevant submesoscale and mesoscale baroclinic instability. Due to the submesoscale nature of the observed dynamics, downwelling occurs more rapidly and in a smaller spatial area than upwelling, and water consequently can remain subducted for days to months due to the aperiodic nature of these dynamics. As a result, there is net subduction of carbon through an episodic flux on the order 100 mg C m^{-2} d^{-1}, as observed, and an integrated downward advective flux of 10 mg C m^{-2} d^{-1} at a depth of 150 m (*SI Appendix*, Fig. S11). Sinking POC flux estimates from time

series observations in the North Atlantic and Western Mediterranean range from 0.3 to 60 mg C m^{-2} d^{-1} (45, 46). The achieved advective export flux is of similar order of magnitude to the average sinking flux and, notably, its inclusion in coarse resolution carbon cycle models or budgets could double the rate of ocean carbon export.

Intrusions occur along density surfaces and the mechanism hinges on mesoscale processes, which set up deep-reaching fronts that increase the potential depth range of export and support episodic submesoscale processes, which accelerate the rate of export and disrupt periodic flows. Together, these increase the likelihood that water parcels are not upwelled after subduction. In regimes where the flow is net restratifying, there will be an associated net subduction of carbon (12). Additionally, in regions with enhanced surface submesoscale dynamics, enhanced subsurface vertical velocity and aperiodic upwelling and downwelling will lead to episodic injection of water parcels that persist subsurface for long time periods (30, 47). Furthermore, rather than persisting at the ACM density surface, modeling efforts indicate that POC can be transported below the depth of downward vertical motion when sinking and advective export occur together (48). Future work should quantify the ways that the depth structure and timescale of vertical transport interact with ecological dynamics and sinking fluxes.

We next assessed the global extent of POC export by intrusions using a physical understanding of their dynamics and a number of data sources including the Bermuda Atlantic Time-series, which
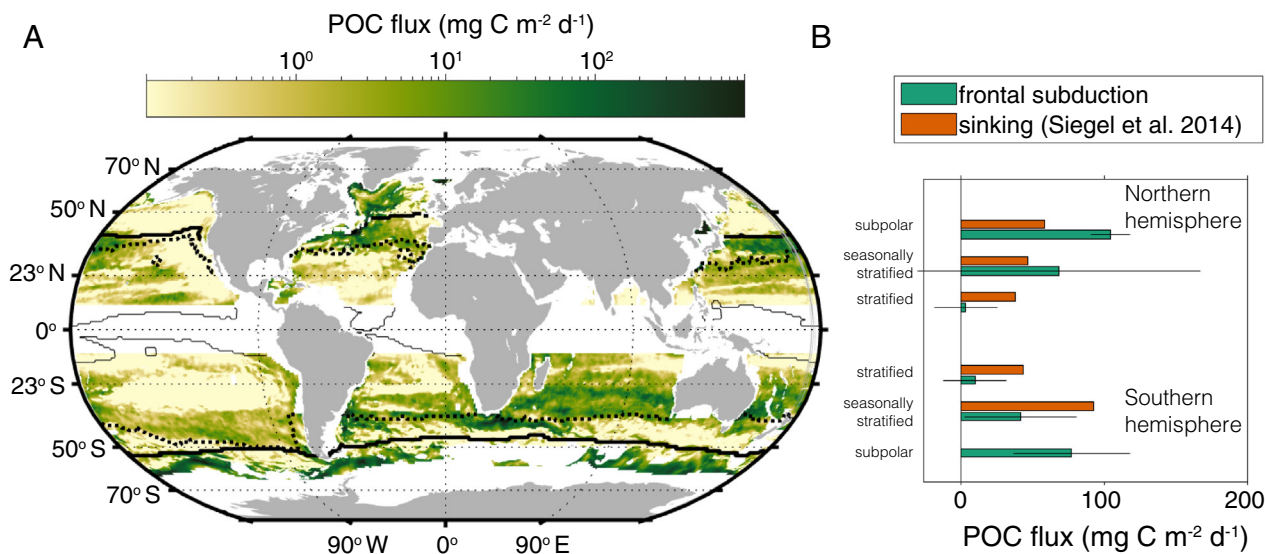
Fig. 5. Global importance of intrusion-driven POC export. (*A*) Global estimate of the magnitude of POC flux due to physically driven intrusions from the base of the photic zone in subtropical and subpolar gyres. The thick line delineates the equatorward limit of the subpolar gyre, the thick dotted line divides the seasonally stratified subtropical gyre from the permanently stratified subtropical gyre, and the thin solid line delineates the equatorward limit of the subtropical gyres. (*B*) Average POC flux from physically driven intrusions grouped into three broad bio-regions in each hemisphere (subpolar, seasonally stratified subtropical [seasonally stratified], and permanently stratified subtropical [stratified]). Error bars on the integrated POC flux represent errors in estimated POC gradients, which can be large due to relatively sparse observations. The subduction flux is compared to the sinking flux at the base of the photic zone as estimated by Siegel et al. (55). There is no error estimate provided for the sinking flux.

characterizes the subtropical ocean water column from the surface to mesopelagic on a monthly basis (49), satellite observations, and the global array of Argo floats (50). Specifically, along-isopycnal transport was estimated using a well-established parameterization of eddy tracer flux (51) and a diffusivity estimate based on recent work that accounts for submesoscale dynamics (52), alongside the global observations (*SI Appendix*, SI Text). We quantify flux as

$$\overline{w'C'} = -\kappa(2S \cdot \nabla_h C + S^2 C_z), \qquad [1]$$

where $\overline{w'C'}$ is the spatial and temporal average vertical flux of POC (*C*) and *S* is the isopycnal slope. The eddy transfer coefficient is given by $\kappa = 0.015 \frac{M^2}{N} l^2$ where M^2 and N^2 are the lateral and vertical buoyancy gradients, respectively (N^2 = db/dz and M^2 = |∇b| with b = –gρ/ρ$_0$, where ρ is seawater density, ρ$_0$ is a constant reference density of 1,027 kg/m^3 and g is the acceleration due to gravity), and *l* is a mixing length (*SI Appendix*, Fig. S10). This is a conservative estimate of carbon flux because it underestimates the influence of submesoscale processes. Several patterns emerged from the global analysis, including a large flux of POC by intrusions in subpolar gyres (Fig. 5), which act in concert with the seasonal mixed layer eddy-driven flux (12). The advective flux of POC in the seasonally stratified subtropical gyres, at ~75 and 50 mg C m^{-2} d^{-1} in northern and southern subtropical gyres, respectively, is larger than previous estimates. Moreover, in 26 y of BATS data, 1.3% of profiles have an ACM that is likely due to intrusions from the photic zone (*SI Appendix*, Fig. S13), lending support to our process model-based estimates. These results establish the global magnitude of the intrusion export process, albeit with order of magnitude uncertainty. Total contributions to POC export will be better constrained with the future acquisition of subsurface POC data alongside high-resolution modeling studies. In addition, the importance of this process calls for improved understanding of vertical transport processes, including quantification of vertical tracer flux (53), and understanding of the coupling

between surface-intensified submesoscale dynamics and subsurface transport (54).

Our analyses indicate that the net intrusion-driven POC flux at 100 m is downward and is of similar magnitude as the sinking flux in subtropical regions (55) (Fig. 5). Current estimates of POC export in subtropical oceans are known to be insufficient when it comes to accounting for heterotrophic production levels in the mesopelagic, or for balancing observed rates of net community production in the photic zone on annual timescales (56, 57). Other physically driven processes including mixed layer eddy subduction (12) and the mixed layer pump (58, 59) do not resolve this imbalance on annual timescales. It should be noted that some global and regional modeling studies also conclude that additional processes beyond sinking flux are needed to close the carbon budget in subtropical systems (60, 61). In addition to the enhanced POC flux, intrusions carry dissolved organic matter thereby contributing to a larger and chemically complex carbon pool at depth (62). Organic carbon export by intrusions is likely critical for closing carbon budgets in subtropical regions. Increased observations of global subsurface carbon distributions coupled with advancements in quantification of vertical tracer flux by coupled mesoscale-submesoscale dynamics will likely be essential to closing the subtropical organic carbon budget.

Conclusions

The coupled ocean biophysical dynamics revealed here transport picophytoplankton and heterotrophic bacteria communities in three-dimensional intrusions from photosynthetically productive sunlit layers to the mesopelagic in subtropical oceans. This constitutes an important contribution to POC export and microbial diversity in the upper mesopelagic of the Mediterranean, and is also relevant globally. The export mechanism operates throughout the year and recruits contributions from the biomass maximum of the photic zone, including the DCM, which was not thought to contribute substantially to export. Many of the small cell size populations that are exported by

intrusion dynamics are unlikely to have other routes into the meso-pelagic as intact cells. By revealing this process, we highlight how the ecology and biogeochemistry of the ocean's interior are influenced by surface-intensified dynamics that are variable on timescales of days to weeks rather than only seasonal timescales.

Transport of photic zone communities to depth in intrusions alters the composition of food supplies and contributes greater functional complexity to mesopelagic ecosystems. Heterotrophic bacteria constitute a large fraction of the microbial POC in intrusions and injection of these communities is ecologically significant because some taxa appear to thrive in the aphotic zone thereby modifying "standard" mesopelagic microbial metabolisms and interactions. Moreover, the oxygen transported within intrusions alongside the dissolved organic carbon and POC will impact the biogeochemistry of the dark ocean, including remineralization and attenuation of organic matter. There is much to be learned about the uncultivated bacteria that are enhanced in the intrusions. As the oceans warm and density stratification intensifies, picophytoplankton are expected to constitute a larger fraction of primary production (6, 7). The physically driven export mechanism described here is predicted to be robust to increasing photic zone stratification and the related selection of smaller-sized taxa that is anticipated in a warming climate. Overall, we show that intrusions are ubiquitous in subtropical oceans, and are responsible for the coupling of photic-zone microbes and production with mesopelagic productivity, biodiversity, and biogeochemical processes.

Materials and Methods

Sampling Strategy. Sampling occurred during three research cruises that took place from July 17 to 24, 2017 on the *R/V SOCIB* (IRENE), May 27 to June 2, 2018 on the *NRV Alliance* (Calypso 2018; CLP18), and March 21 to April 12, 2019 on the *NO Pourquoi Pas?* (Calypso 2019; CLP19) (63).

Ship transects were oriented perpendicular to the largest buoyancy and velocity gradients to the extent possible. This sampling design aimed to capture the greatest degree of variability in water masses and isopycnal depth range. Each transect was completed as rapidly as possible. On transects where CTD casts were performed to sample water (Fig. 1*A*), there were 30 min to 1 h between casts on a given transect. 3 to 8 CTD casts were conducted in each cross-frontal transect reported here, at a spacing of 1 to 10 km. These transects were completed in 3 to 6 h. CTD cast locations were chosen based on cross-front underway CTD (UCTD) (64) or EcoCTD (65) measurements performed along the same cross-front section immediately prior to the CTD transect. Samples were collected at six depths using Niskin bottles mounted to a CTD rosette. On every cast, samples were collected at 6 depths. These were selected based on the following criteria: i) near the surface at a fixed depth of 5 m; ii) within the mixed layer (~25 m); iii) the chlorophyll maximum, i.e., either the DCM or the base of the mixed layer; iv) just below the chlorophyll maximum; v) the secondary, aphotic chlorophyll maximum (ACM) if present, or a fixed depth of 120 m if not present; vi) the maximum cast depth (200 m in 2017 and 2019, 250 m in 2018). On three of the transects, community composition data are not available, but we use nutrient, CTD, and bio-optical observations.

Hydrographic Observations. Temperature and salinity were measured with a dual Seabird SBE9 on the CTD rosette. Near continuous profiling was carried out with an *Oceansciences* underway-CTD or the EcoCTD. The UCTD, a custom SBE sensor that samples at 16 Hz. The EcoCTD measures conductivity, temperature, and pressure with an RBR*concerto*[3] inductive CTD (65). The data processing from the underway instruments is described in Dever et al. (66). Discrete samples were taken to calibrate the SBE9. The UCTD was calibrated immediately prior to the cruise by Seabird. The EcoCTD was calibrated by RBR immediately prior to the cruise and the optical instruments were cross-calibrated by mounting it to the CTD rosette frame for one cast during each cruise. Velocity was observed using a vessel-mounted acoustic Doppler current profiler (ADCP) on each cruise.

Bio-Optical Observations. Chlorophyll in vivo fluorescence was measured by a Chelsea Aqua 3 fluorometer (CLP18) and WETLabs ECO-AFL/FL (CLP19) mounted on the CTD and a WETLabs ECOPuck on the EcoCTD. In vivo fluorescence was calibrated with in situ samples collected from the fluorescence maximum and at the maximum profile depth (200 or 250 m). For each sample, 0.5 L of seawater was filtered on board through a 45 mm GF/F Whatman filter. Concentrations of chl *a* were determined using the fluorometric method described in ref. 67, total pigment extracted with 90% acetone for 24 h at 4 °C in the dark and determined with a fluorometer (Turner Designs).

Oxygen was measured by a Seabird SBE43 oxygen sensor mounted to the CTD and a RINKO III oxygen sensor on the EcoCTD. The output of the oxygen sensors was calibrated against Winkler titrations performed at sea within 48 h of sampling (Metrohm 888 Titrator).

Biological Community Composition.
DNA extraction, PCR, and sequencing. DNA samples for characterizing microbial communities were obtained by filtering biomass from 500 mL of natural seawater onto 47 mm 0.2 μm pore size polyethersulfone membrane filters (Supor 200, Pall Gelman). Filters were placed into sterile cryovials, flash-frozen in liquid nitrogen, and transferred to −80 °C until extraction using the DNeasy Plant Kit (Qiagen), with a modification including a bead beating step (68). During the 2017 and 2018 cruises, samples were stored in liquid nitrogen for the duration of the cruise after which they were stored at −80 °C until extraction. DNA was amplified using the primers 27FB (5′-AGRGTTYGATYMTGGCTCAG3′) and 338RPL (5′-GCWGGCCWCCCGTAGGWGT-3′) (69, 70) targeting the V1-V2 hypervariable region of the 16S rRNA gene with Illumina adapters, allowing us to explore the diversity of eukaryotic phytoplankton (via plastid 16S rRNA gene), cyanobacteria, and heterotrophic bacterioplankton (28, 69–71). PCRs contained 25 ng of template, 5 μL of 10× buffer, 1 U of HiFi-Taq, 1.6 mM $MgSO_4$ (Thermo Fisher) and 0.2 μM of each primer. The PCR cycling parameters were 94 °C for 2 min; 30×94 °C for 15 s, 55 °C for 30 s, 68 °C for 1 min, and a final elongation at 68 °C for 7 min. Paired-end library sequencing (2 × 300 bp) was performed using the Illumina MiSeq platform.
16S rRNA gene amplicon analyses. Sequences were demultiplexed and assigned to corresponding samples using CASAVA (Illumina). A 10 bp running window was utilized to trim low-quality sequence ends at a Phred quality (Q) of 25 using Sickle 1.33 (72). Paired-end reads were merged using USEARCH v10.0.240 (73) when reads had a ≥ 50 bp overlap with maximum 5% mismatch. The merged reads were then filtered to remove reads with maximum error rate > 0.001 or shorter than 200 bp. Only sequences with an exact match to both primers were kept and primer sequences were trimmed using Cutadapt v.1.13 (74). After removal of single sequence reads, the average number of amplicon reads from the 317 samples was 259,104 ± 133,685.

Cyanobacterial and plastid amplicons were initially parsed using the phylogenetic pipeline in PhyloAssigner v.6.166 (69). Amplicons from plastids and cyanobacteria were further classified using a global plastid and cyanobacterial reference alignment and tree according to protocols outlined in Choi et al. (71). Cyanobacterial amplicons were analyzed using fine-scale cyanobacterial reference alignment and tree (70), and plastid amplicons were further analyzed using multiple high-resolution alignments and trees focusing on stramenopiles and viridiplantae (32, 71).

For the assessment of heterotrophic bacterioplankton communities, sequences (82,135,874 reads) were resolved into 49,150 ASVs of 100% pairwise identity with USEARCH v10.0.240 (73). Taxonomies were assigned to each ASV using classify-sklearn by QIIME2 (75) searching against the SILVA database release 138 (76).
Cell quantification. We preserved samples for quantification by flow cytometry from the same Niskin bottles from which we took the samples for DNA extraction. Samples were preserved using 10 μL of EM grade 25% Glutaraldehyde per 1 mL seawater and then flash frozen in liquid nitrogen (or at −80° for casts 1 to 19 in 2019). Samples were then stored at −80 °C until analysis. Cells were quantified using a BD Influx flow cytometer equipped with a 488 nm laser. Forward angle light scatter, side scatter, and autofluorescence at 692/40 nm, 572/27 nm, and 520/35 nm were recorded. Photosynthetic cells were counted by triggering on forward angle light scatter. Calibration beads were added to each sample immediately before analysis (0.75 μm yellow-green, Polysciences, Inc and 1.0 to 1.4 μm ultrarainbow, Spherotech). Each sample was run for 8 min at 25 μL min⁻¹ after a prerun of 2 min. Heterotrophic bacteria cells were counted by staining samples with SYBR Green and triggering on autofluorescence at 520 nm. Samples were run for 4 min after a 2-min prerun. Analysis was performed in WinList (Verity Software House).

Integrating the constrained gene copy numbers in cyanobacteria to examine specific clade abundances (70) allowed us to leverage flow cytometric data to examine contributions of specific *Prochlorococcus* and *Synechococcus* clades (this analysis was not performed for picoeukaryotes due to having unknown rRNA gene copy numbers).

Statistical Analysis of Community Composition. The hierarchical clustering presented in the main text was performed using the "ggdendro" package and average clustering and Manhattan distance. In all cases, intrusion samples refer to the aphotic portion of intrusions, unless otherwise specified. This is defined as deeper than 90 m, using the maximum 1% light level across all observations.

We test which ASVs have statistically significant different abundances (differentially abundant) between sample groups using ANCOM implemented in Qiime2. We define three groups for this analysis: the chlorophyll maximum on the dense side of the front and intrusion samples shallower than 90 m (origin waters), the samples in the aphotic zone in intrusions (deeper than 90 m), and samples in the background deeper than 90 m. ANCOM assumes that fewer than 25% of the ASVs change between groups (77).

Estimating POC. We estimate the POC concentration using multiple complementary methods. Each captures a different contribution to the POC.
Flow cytometry. We use literature values (78, 79) to estimate the carbon content of the cells enumerated by flow cytometry. The values we use are 39, 82, and 530 fg C cell^{-1} for *Prochlorococcus, Synechococcus,* and picoeukaryotes, respectively. The carbon per cell is most uncertain for the picoeukaryotes, which have the largest biomass per cell and are a large contributor to the small photosynthetic community during the 2019 cruise, and for the diverse heterotrophic bacteria community. Following ref. 39, we use a value of 20 fg C cell^{-1} for heterotrophic bacteria.
Optical instruments. The particle beam attenuation is a proxy for particles in the size range 5 to 20 μm (24). The beam transmission (Tr) (Seatech/Chelsea in 2018, WETlabs in 2019) was measured and used to derive c_p as

$$c_p = \frac{1}{0.25} \, ln \, \frac{Tr}{100}. \qquad [2]$$

The community composition, in addition to the total POC, may affect c_p. The beam attenuation is affected by phytoplankton and also by bacteria, zooplankton, and detritus. It is not currently possible to measure beam transmission on the EcoCTD. Instead, the EcoCTD measures backscatter at 700 nm. Both the beam attenuation and backscatter can be converted to carbon using region-specific empirical calibrations. We use a correlation between c_p and POC of 1.78 m^2(g C)$^{-1}$ (80). The range of possible values used for uncertainty estimates includes the values reported in ref. 81. We use a relationship between backscatter and POC (POC = 54,463 × b_{bp} − 1.19 mg C m^{-3}) (82).

Definition of Intrusion ACMs. Intrusions are identified as an ACM.

1. The ACM must extend at least 5 m in the vertical. The bounds of the intrusion are set by the bounds of the elevated chlorophyll concentration. *There are thermohaline intrusions that are not associated with elevated chlorophyll concentration. These are intrusions in a more general sense but are not included in the analysis here because they do not necessarily contribute more to carbon export than the background waters.*
2. ACMs must be present contiguously, in more than one CTD cast within a transect to constitute an intrusion. The intrusion must be below 100 m in at least one cast along the transect. The intrusion must occupy the same density range across the front. *This criterion allows us to confidently identify thin intrusions (small vertical extent) over large lateral scales. In addition, we are able to approximate the origins of the intrusions within the euphotic zone. By contrast, when identifying intrusions from isolated profiles (83) investigators were only able to identify intrusions that were already below 100 m and at least 150 m in vertical extent.*
3. The ACM is associated with an inversion in the vertical in at least one other property (temperature, salinity, oxygen, POC). *This criterion helps to ensure that the ACM is due to an intrusion rather than local growth or sinking of phytoplankton. Within an intrusion, the gradients in chlorophyll and the other properties may not be aligned due to patchiness in the origin location.*

Process Study Model. The POC flux is computed using process study models initialized with a cross-section across the Almería-Oran front. Two configurations of the PSOM (84, 85) are run with one representing a stratified summer period and the other the springtime period when the thermocline density surface outcrop at the sea surface (30). The initial condition representing the springtime period is obtained by cooling the sea surface and using convective adjustment until the mixed layer has a maximum depth of 70 m. The models are re-entrant channels with walls at north–south boundaries and periodic boundaries in the east-west direction. The model domain is centered at 36.9°N, extends 128 km in the east-west direction, 216 km in the north-south direction, and is 1 km deep. The models have grid spacing of 500 m with a stretched grid in the north–south direction that attains a spacing of 2 km within 40 km of the southern and northern solid boundaries. There are 64 vertical levels on a stretched grid with grid spacing ranging from 0.5 m at the surface to 54 m at depth. The model timestep is 108 s. The horizontal diffusion is 1 m^2/s. The vertical diffusion has a constant value of 10^{-5} m^2/s. The model has a flat bottom and a linear bottom drag of 10^{-4} m/s. The POC flux is computed by evolving the mean POC profile from each season for a month with no reactions or restoring.

Eddy Flux Parameterization. To approximate the global magnitude of POC export due to the intrusion process described in this paper, we parameterize the vertical flux using a skew flux (51, 86)

$$\overline{w'C'} = -\kappa(2S \cdot \nabla_h C + S^2 C_z), \qquad [3]$$

where w is the vertical velocity, C is the POC concentration, and S is the isopycnal slope. The isopycnal slope is a 2D vector and is computed from a monthly Argo climatology (87). This climatology has a resolution of 56 km near the equator and increases to 22.5 km at 66.5° and poleward. The isopycnal slope term in this expression accounts for the effect of a limited depth range of sloping isopycnal surfaces. The flux will go to zero if an isopycnal is flat. We use an eddy transfer coefficient given by $\kappa = 0.015 \frac{M^2}{N} l^2$. This eddy transfer coefficient was derived by Visbeck et al. (86) based on linear stability analysis of baroclinic eddies. The transfer coefficient, which has units of m^{2}s^{-1}, is given by an eddy velocity multiplied by a mixing length (l). The eddy velocity is determined to be $\alpha Ri^{-1/2}f$. It is notable that the coefficient $\alpha Ri^{-1/2}$ is the scaling derived by Freilich and Mahadevan (52) for the proportion of the vertical motion that is along sloping isopycnal surfaces. This observation further supports the use of this scaling for the vertical eddy flux. We use the constant $\alpha = 0.015$ (52, 86). The coefficient $\alpha \frac{M^2}{N}$ is computed from a monthly climatology of Argo profiles (87, 88). We quantify the mixing length from the variance of salinity on an isopycnal surface as $l = \frac{[<\Pi'\Pi'>]^{1/2}}{[<|\nabla\Pi|>]}$ where $\Pi' = \Pi - <\Pi>$ after Cole et al. (89). All gradients and the mixing length are computed on a 1-degree grid using Argo data. A single annual value is used for the mixing length and monthly values are used for $\alpha \frac{M^2}{N}$. The average values are shown in *SI Appendix*, Fig. S10.

The POC gradients are computed from a climatology of POC based on Biogeochemical Argo data and satellite observations combined with a neural network to create 3D fields and 0.25° resolution with 36 vertical levels between the surface and 1,000 m (90). The POC flux is averaged over all data points where the density difference between the surface and the euphotic depth is at least 0.3 kg m^{-3}, indicating that the base of the euphotic zone is stratified.

Data, Materials, and Software Availability. Hydrographic data displayed in the figures is available at https://dx.doi.org/10.5281/zenodo.10871048 and sequences with all metadata are available at BioSample accession numbers SAMN40603493-SAMN40603806. Previously published data were used for this work (88–90).

Author affiliations: [a]Massachusetts Institute of Technology-Wood Hole Oceanographic Institution Joint Program in Oceanography, Woods Hole, MA 02543; [b]Scripps Institution of Oceanography, University of California San Diego, La Jolla, CA 92093; [c]Department of Earth, Environmental, and Planetary Sciences, Brown University, Providence, RI 02912; [d]Division of Applied Mathematics, Brown University, Providence, RI 02912; [e]GEOMAR—Helmholtz Centre for Ocean Research, Kiel 24105, Germany; [f]Department of Physical Oceanography, Woods Hole Oceanographic Institution, Woods Hole, MA 02543; [g]Sistema de Observación y Predicción Costero de las Illes Balears (SOCIB), Palma de Mallorca 07121, Spain; [h]Physical & Biological Sciences Division, University of California, Santa Cruz, CA 95064; [i]Instituto Mediterraneo de Estudios Avanzados (IMEDEA), Esporles 07190, Spain; [j]Applied Physics Lab, University of Washington, Seattle, WA 98105; and [k]Marine Biological Laboratory, Woods Hole, MA 02543

1. F. P. Chavez, M. Messié, J. T. Pennington, Marine primary production in relation to climate variability and change. *Annu. Rev. Mar. Sci.* **3**, 227–260 (2011).
2. C. Lopes, M. Kucera, A. C. Mix, Climate change decouples oceanic primary and export productivity and organic carbon burial. *Proc. Natl. Acad. Sci. U.S.A.* **112**, 332–335 (2015).
3. D. A. Siegel, T. DeVries, I. Cetinić, K. Bisson, Quantifying the ocean's biological pump and its carbon cycle impacts on global scales. *Annu. Rev. Mar. Sci.* **15**, 329–356 (2023).
4. S. J. Biller, P. M. Berube, D. Lindell, S. W. Chisholm, Prochlorococcus: The structure and function of collective diversity. *Nat. Rev. Microbiol.* **13**, 13–27 (2015).
5. A. Z. Worden et al., Rethinking the marine carbon cycle: Factoring in the multifarious lifestyles of microbes. *Science* **347**, 1257594 (2015).
6. M. J. Behrenfeld et al., Climate-driven trends in contemporary ocean productivity. *Nature* **444**, 752–755 (2006).
7. P. Flombaum et al., Present and future global distributions of the marine Cyanobacteria *Prochlorococcus* and *Synechococcus*. *Proc. Natl. Acad. Sci. U.S.A.* **110**, 9824–9829 (2013).
8. T. L. Richardson, G. A. Jackson, Small phytoplankton and carbon export from the surface ocean. *Science* **315**, 838–840 (2007).
9. F. De Martini, S. Neuer, D. Hamill, J. Robidart, M. W. Lomas, Clade and strain specific contributions of *Synechococcus* and *Prochlorococcus* to carbon export in the Sargasso Sea. *Limnol. Oceanogr.* **63**, S448–S457 (2018).
10. L. Guidi et al., Plankton networks driving carbon export in the oligotrophic ocean. *Nature* **532**, 465–470 (2016).
11. C. Bachy et al., Phytoplankton surveys in the Arctic Fram Strait demonstrate the tiny Eukaryotic Alga Micromonas and other Picoprasinophytes contribute to deep sea export. *Microorganisms* **10**, 961 (2022).
12. M. M. Omand et al., Eddy-driven subduction exports particulate organic carbon from the spring bloom. *Science* **348**, 222–225 (2015).
13. M. R. Stukel et al., Mesoscale ocean fronts enhance carbon export due to gravitational sinking and subduction. *Proc. Natl. Acad. Sci. U.S.A.* **114**, 1252–1257 (2017).
14. J. Callies, R. Ferrari, J. M. Klymak, J. Gula, Seasonality in submesoscale turbulence. *Nat. Commun.* **6**, 1–8 (2015).
15. S. Fielding et al., Mesoscale subduction at the Almeria-Oran front: Part 2. Biophysical interactions. *J. Mar. Syst.* **30**, 287–304 (2001).
16. S. Ruiz et al., Effects of oceanic mesoscale and submesoscale frontal processes on the vertical transport of phytoplankton. *J. Geophys. Res. Oceans* **124**, 5999–6014 (2019).
17. J. Rodriguez et al., Mesoscale vertical motion and the size structure of phytoplankton in the ocean. *Nature* **410**, 360–363 (2001).
18. D. L. Rudnick, N. D. Zarokanellos, J. Tintoré, A four-dimensional survey of the Almeria-Oran front by underwater gliders: Tracers and circulation. *J. Phys. Oceanogr.* **52**, 225–242 (2022).
19. M. Lévy, P. Klein, A.-M. Treguier, Impact of sub-mesoscale physics on production and subduction of phytoplankton in an oligotrophic regime. *J. Mar. Res.* **59**, 535–565 (2001).
20. M. A. Spall, Frontogenesis, subduction, and cross-front exchange at upper ocean fronts. *J. Geophys. Res. Oceans* **100**, 2543–2557 (1995).
21. R. T. Pollard, L. A. Regier, Vorticity and vertical circulation at an ocean front. *J. Phys. Oceanogr.* **22**, 609–625 (1992).
22. J. A. Barth et al., Injection of carbon from the shelf to offshore beneath the euphotic zone in the California Current. *J. Geophys. Res. Oceans* **107**, 10-1–10-8 (2002).
23. R. M. Morris, C. D. Frazar, C. A. Carlson, Basin-scale patterns in the abundance of SAR11 subclades, marine Actinobacteria (OM1), members of the Roseobacter clade and OCS116 in the South Atlantic. *Environ. Microbiol.* **14**, 1133–1144 (2012).
24. I. M. Deutschmann et al., Disentangling temporal associations in marine microbial networks. *Microbiome* **11**, 83 (2023).
25. A. K. Hawley et al., Diverse Marinimicrobia bacteria may mediate coupled biogeochemical cycles along eco-thermodynamic gradients. *Nat. Commun.* **8**, 1507 (2017).
26. J. T. Allen, D. Smeed, J. Tintoré, S. Ruiz, Mesoscale subduction at the Almeria-Oran front: Part 1: Ageostrophic flow. *J. Mar. Syst.* **30**, 263–285 (2001).
27. E. Marañón et al., Deep maxima of phytoplankton biomass, primary production and bacterial production in the Mediterranean Sea. *Biogeosciences* **18**, 1749–1767 (2021).
28. S. J. Giovannoni, K. L. Vergin, Seasonality in ocean microbial communities. *Science* **335**, 671–676 (2012).
29. A. Coe et al., Coping with darkness: The adaptive response of marine picocyanobacteria to repeated light energy deprivation. *Limnol. Oceanogr.* **66**, 3300–3312 (2021).
30. M. Freilich, A. Mahadevan, Coherent pathways for subduction from the surface mixed layer at ocean fronts. *J. Geophys. Res. Oceans* **126**, e2020JC017042 (2021).
31. E. Cutolo et al., Diagnosing frontal dynamics from observations using a variational approach. *J. Geophys. Res. Oceans* **127**, e2021JC018336 (2022).
32. C. J. Choi et al., Seasonal and geographical transitions in eukaryotic phytoplankton community structure in the Atlantic and Pacific Oceans. *Front Microbiol.* **11**, 2187 (2020).
33. C. García-Gómez et al., Shifts in the protist community associated with an anticyclonic gyre in the Alboran Sea (Mediterranean Sea). *FEMS Microbiol. Ecol.* **96**, fiaa197 (2020).
34. D. M. Karl, M. J. Church, Microbial oceanography and the Hawaii Ocean Time-series programme. *Nat. Rev. Microbiol.* **12**, 699–713 (2014).
35. M. V. Zubkov, M. A. Sleigh, P. H. Burkill, R. J. G. Leakey, Picoplankton community structure on the Atlantic Meridional Transect: A comparison between seasons. *Progr. Oceanogr.* **45**, 369–386 (2000).
36. G. J. Herndl, B. Bayer, F. Baltar, T. Reinthaler, Prokaryotic life in the deep ocean's water column. *Annu. Rev. Mar. Sci.* **15**, 461–483 (2023).
37. G. Bratbak, Bacterial biovolume and biomass estimations. *Appl. Environ. Microbiol.* **49**, 1488–1493 (1985).
38. H. W. Ducklow, Bacterial production and biomass in the oceans. *Microbial. Ecol. Oceans* **1**, 85–120 (2000).
39. S. Lee, J. A. Fuhrman, Relationships between biovolume and biomass of naturally derived marine bacterioplankton. *Appl. Environ. Microbiol.* **53**, 1298–1303 (1987).
40. L. H. Orellana et al., Verrucomicrobiota are specialist consumers of sulfated methyl pentoses during diatom blooms. *ISME J.* **16**, 630–641 (2022).
41. C. E. Nelson, C. A. Carlson, C. S. Ewart, E. R. Halewood, Community differentiation and population enrichment of Sargasso Sea bacterioplankton in the euphotic zone of a mesoscale mode-water eddy: Bacterioplankton in a Sargasso Sea mode-water eddy. *Environ. Microbiol.* **16**, 871–887 (2014).
42. T. Severin et al., Impact of an open-sea convection event (0–1500 m) on prokaryotic diversity and activity in the NW Mediterranean Sea. *Environ. Microbiol.* **18**, 4378–4390 (2016).
43. A. E. Maas et al., Migratory zooplankton excreta and its influence on prokaryotic communities. *Front. Mar. Sci.* **7**, 573268 (2020).
44. M. Mestre et al., Sinking particles promote vertical connectivity in the ocean microbiome. *Proc. Natl. Acad. Sci. U.S.A.* **115**, E6799–E6807 (2018).
45. J.-C. Miquel et al., Dynamics of particle flux and carbon export in the northwestern Mediterranean Sea: A two decade time-series study at the DYFAMED site. *Progr. Oceanogr.* **91**, 461–481 (2011).
46. S. A. Owens et al., A new time series of particle export from neutrally buoyant sediments traps at the Bermuda Atlantic Time-series Study site. *Deep Sea Res., Part I: Oceanogr. Res. Pap.* **72**, 34–47 (2013).
47. S. Ramachandran, A. Tandon, A. Mahadevan, Enhancement in vertical fluxes at a front by mesoscale-submesoscale coupling. *J. Geophys. Res. Oceans* **119**, 8495–8511 (2014).
48. M. Dever, D. Nicholson, M. M. Omand, A. Mahadevan, Size-differentiated export flux in different dynamical regimes in the ocean. *Global Biogeochem. Cycles* **35**, e2020GB006764 (2021).
49. M. W. Lomas, N. R. Bates, R. J. Johnson, D. K. Steinberg, T. Tanioka, Adaptive carbon export response to warming in the Sargasso Sea. *Nat. Commun.* **13**, 1211 (2022).
50. F. Chai et al., Monitoring ocean biogeochemistry with autonomous platforms. *Nat. Rev. Earth Environ.* **1**, 315–326 (2020).
51. P. R. Gent, J. C. Mcwilliams, Isopycnal mixing in ocean circulation models. *J. Phys. Oceanogr.* **20**, 150–155 (1990).
52. M. Freilich, A. Mahadevan, Decomposition of vertical velocity for nutrient transport in the upper ocean. *J. Phys. Oceanogr.* **49**, 1561–1575 (2019).
53. C. P. Spingys et al., Observations of nutrient supply by mesoscale eddy stirring and small-scale turbulence in the oligotrophic North Atlantic. *Global Biogeochem. Cycles* **35**, e2021GB007200 (2021).
54. Y. Luo, J. Callies, Vertical exchange induced by mixed layer instabilities. *J. Phys. Oceanogr.* **53**, 2701–2716 (2023).
55. D. A. Siegel et al., Global assessment of ocean carbon export by combining satellite observations and food-web models. *Global Biogeochem. Cycles* **28**, 181–196 (2014).
56. S. L. C. Giering et al., Reconciliation of the carbon budget in the ocean's twilight zone. *Nature* **507**, 480–483 (2014).
57. F. Baltar, J. Arístegui, J. M. Gasol, G. J. Herndl, Microbial functioning and community structure variability in the mesopelagic and epipelagic waters of the subtropical Northeast Atlantic Ocean. *Appl. Environ. Microbiol.* **78**, 3309–3316 (2012).
58. G. Dall'Olmo, J. Dingle, L. Polimene, R. J. W. Brewin, H. Claustre, Substantial energy input to the mesopelagic ecosystem from the seasonal mixed-layer pump. *Nat. Geosci.* **9**, 820–823 (2016).
59. P. W. Boyd, H. Claustre, M. Levy, D. A. Siegel, T. Weber, Multi-faceted particle pumps drive carbon sequestration in the ocean. *Nature* **568**, 327–335 (2019).
60. L. Resplandy, M. Lévy, D.J. McGillicuddy Jr., Effects of Eddy-driven subduction on ocean biological carbon pump. *Global Biogeochem. Cycles* **33**, 1071–1084 (2019).
61. M. Nowicki, T. DeVries, D. A. Siegel, Quantifying the carbon export and sequestration pathways of the ocean's biological carbon pump. *Global Biogeochem. Cycles* **36**, e2021GB007083 (2022).
62. M. A. Moran et al., The Ocean's labile DOC supply chain. *Limnol. Oceanogr.* **67**, 1007–1021 (2022).
63. A. Mahadevan et al., "CALYPSO 2019 Cruise Report: Field campaign in the Mediterranean" (WHOI Tech. Rep. WHOI-2020-01, 2020), https://hdl.handle.net/1912/25266. https://doi.org/10.1575/1912/25266.
64. D. L. Rudnick, J. Klinke, The underway conductivity–temperature–depth instrument. *J. Atmos. Ocean. Technol.* **24**, 1910–1923 (2007).
65. M. Dever et al., EcoCTD for profiling oceanic physical–biological properties from an underway ship. *J. Atmosph. Ocean. Technol.* **37**, 825–840 (2020).
66. M. Dever et al., UCTD and EcoCTD Observations from the CALYPSO Pilot Experiment (2018): Cruise and Data Report (Woods Hole Oceanographic Institution, 2019).
67. T. R. Parsons, Y. Maita, C. M. Lalli, "Fluorometric determination of chlorophylls" in *A Manual of Chemical & Biological Methods for Seawater Analysis*, T. R. Parsons, Y. Maita, C. M. Lalli, Eds. (Pergamon, 1984), pp. 107–109.
68. E. Demir-Hilton et al., Global distribution patterns of distinct clades of the photosynthetic picoeukaryote *Ostreococcus*. *ISME J.* **5**, 1095–1107 (2011).
69. K. Vergin, B. Done, C. Carlson, S. Giovannoni, Spatiotemporal distributions of rare bacterioplankton populations indicate adaptive strategies in the oligotrophic ocean. *Aquat. Microb. Ecol.* **71**, 1–13 (2013).
70. S. Sudek et al., Cyanobacterial distributions along a physico-chemical gradient in the Northeastern Pacific Ocean. *Environ. Microbiol.* **17**, 3692–3707 (2015).
71. C. J. Choi et al., Newly discovered deep-branching marine plastid lineages are numerically rare but globally distributed. *Curr. Biol.* **27**, R15–R16 (2017).
72. N. Joshi, J. Fass, Sickle: A sliding-window, adaptive, quality-based trimming tool for FastQ files (Version 1.33) [Software] (2011).
73. R. C. Edgar, H. Flyvbjerg, Error filtering, pair assembly and error correction for next-generation sequencing reads. *Bioinformatics* **31**, 3476–3482 (2015).
74. M. Martin, Cutadapt removes adapter sequences from high-throughput sequencing reads. *EMBnet J.* **17**, 10–12 (2011).

75. N. A. Bokulich et al., Optimizing taxonomic classification of marker-gene amplicon sequences with QIIME 2's q2-feature-classifier plugin. *Microbiome* **6**, 1–17 (2018).
76. C. Quast et al., The SILVA ribosomal RNA gene database project: Improved data processing and web-based tools. *Nucl. Acids Res.* **41**, D590–D596 (2012).
77. S. Mandal et al., Analysis of composition of microbiomes: A novel method for studying microbial composition. *Microbial. Ecol. Health Dis.* **26**, 27663 (2015).
78. A. Z. Worden, J. K. Nolan, B. Palenik, Assessing the dynamics and ecology of marine picophytoplankton: The importance of the eukaryotic component. *Limnol. Oceanogr.* **49**, 168–179 (2004).
79. E. T. Buitenhuis et al., Picophytoplankton biomass distribution in the global ocean. *Earth Syst. Sci. Data* **4**, 37–46 (2012).
80. K. Oubelkheir, H. Claustre, A. Sciandra, M. Babin, Bio-optical and biogeochemical properties of different trophic regimes in oceanic waters. *Liminol. Oceanogr.* **50**, 1795–1809 (2005).
81. R. Rasse et al., Evaluating optical proxies of particulate organic carbon across the surface Atlantic Ocean. *Front. Mar. Sci.* **4**, 367 (2017).
82. N. Mayot et al., Physical and biogeochemical controls of the phytoplankton blooms in North Western Mediterranean sea: A multiplatform approach over a complete annual cycle (2012–2013 DEWEX Experiment). *J. Geophys. Res. Oceans* **122**, 9999–10019 (2017).
83. J. Llort et al., Evaluating Southern Ocean carbon eddy-pump from biogeochemical-argo floats. *J. Geophys. Res. Oceans* **123**, 971–984 (2018).
84. A. Mahadevan, J. Oliger, R. Street, A nonhydrostatic mesoscale ocean model. Part I: Well-posedness and scaling. *J. Phys. Oceanogr.* **26**, 1868–1880 (1996).
85. A. Mahadevan, J. Oliger, R. Street, A nonhydrostatic mesoscale ocean model. Part II: Numerical implementation. *J. Phys. Oceanogr.* **26**, 1881–1900 (1996).
86. M. Visbeck, J. Marshall, T. Haine, M. Spall, Specification of Eddy transfer coefficients in coarse-resolution ocean circulation models. *J. Phys. Oceanogr.* **27**, 381–402 (1997).
87. F. Gaillard, T. Reynaud, V. Thierry, N. Kolodziejczyk, K. von Schuckmann, In situ–based reanalysis of the global ocean temperature and salinity with ISAS: Variability of the heat content and steric height. *J. Clim.* **29**, 1305–1323 (2016).
88. K. Nicolas, P.-M. Annaig, G. Fabienne, *ISAS Temperature and Salinity Gridded Fields* (SEANOE, 2021).
89. S. T. Cole, C. Wortham, E. Kunze, W. B. Owens, Eddy stirring and horizontal diffusivity from Argo float observations: Geographic and depth variability. *Geophys. Res. Lett.* **42**, 3989–3997 (2015).
90. R. Sauzède et al., A neural network-based method for merging ocean color and Argo data to extend surface bio-optical properties to depth: Retrieval of the particulate backscattering coefficient. *J. Geophys. Res. Oceans* **121**, 2552–2571 (2016).